A Stokes-residual backflow stabilization method applied to physiological flows

Cristóbal Bertoglio [a,b], Alfonso Caiazzo [c,*]

[a] Center for Mathematical Modeling, Universidad de Chile, Chile
[b] Institute for Computational Mechanics, Technische Universität München, Germany
[c] Weierstrass Institute for Applied Analysis and Stochastic, Leibniz Institute in Forschungsverbund Berlin e.V. (WIAS), Berlin, Germany

A B S T R A C T

In computational fluid dynamics, the presence of incoming flow at open boundaries (*backflow*) might often yield unphysical oscillations and instabilities issues, even for moderate Reynolds numbers. It is widely accepted that this problem is caused by the incoming convective energy at the open boundary, which cannot be controlled *a priori* when the velocity at the boundary is unknown. In this work, we propose a stabilized finite element formulation for the incompressible Navier–Stokes equations, in which the stabilization term is based on the residual of a weak Stokes problem normal to the open boundary, driven by an approximated boundary pressure gradient. In particular, the viscous term introduces additional dissipation which controls the incoming convective energy. This method has the advantage as it does not require modifications or extensions of the computational domain. Moreover, it does not require a priori assumptions on the shape of the boundary velocity field. We illustrate our approach through several numerical examples relevant to blood and respiratory flows, including Womersley flows and realistic geometries coming from medical imaging. The performance of the simulations is compared to recently reported approaches.

© 2016 Elsevier Inc. All rights reserved.

1. Introduction

1.1. Problem setting

Let us consider a domain $\Omega \subset \mathbb{R}^d$, $d = 2, 3$, whose boundary is decomposed as

$$\partial\Omega := \Gamma_D \cup \Gamma_N \cup \Sigma,$$

in a Dirichlet boundary, a Neumann boundary and a no-slip wall. Furthermore, let us assume that the Neumann boundary is made of n_b disjoint surfaces, i.e. $\Gamma_N = \Gamma_1 \cup \cdots \cup \Gamma_{n_b}$, with $\Gamma_i \cap \Gamma_j = \emptyset$ for $i \neq j$. We consider an incompressible, Newtonian fluid in the domain Ω, modeled in a time interval $[0, T]$ through the Navier–Stokes equations in convective form for the velocity $\boldsymbol{u}(t) : \Omega \to \mathbb{R}^d$ and the pressure $p(t) : \Omega \to \mathbb{R}$:

$$\begin{cases} \rho \partial_t \boldsymbol{u} + \rho \boldsymbol{u} \cdot \nabla \boldsymbol{u} - \mu \Delta \boldsymbol{u} + \nabla p = \boldsymbol{0} & \text{in} \quad \Omega, \\ \nabla \cdot \boldsymbol{u} = 0 & \text{in} \quad \Omega, \\ \boldsymbol{u} = \boldsymbol{u}_{\mathrm{D}} & \text{on} \quad \Gamma_{\mathrm{D}}, \\ \boldsymbol{u} = \boldsymbol{0} & \text{on} \quad \Sigma, \\ \mu \partial_{\boldsymbol{n}} \boldsymbol{u} - p \boldsymbol{n} = -P_k \boldsymbol{n} & \text{on} \quad \Gamma_k, \ k = 1, \dots, n_b, \end{cases} \tag{1}$$

where ρ and μ are the fluid density and dynamic viscosity, respectively. In (1), the Dirichlet data $\boldsymbol{u}_{\mathrm{D}}$ is a known velocity field on the boundary Γ_{D}.

In physiologically realistic blood- and airflow simulations, the Neumann data P_k on the *open boundary* Γ_k are often computed dynamically via so-called *lumped-parameter models* (LPM), see e.g. [20,30,31,34], which relate the boundary pressures to the boundary flow rates, in order to take into account the effect of the downstream domain. In its most general form, a LPM consists of several interconnected zero-dimensional compartments where the dynamics is defined by a system of ordinary differential–algebraic equations of the type

$$\begin{cases} \mathbf{C} \dfrac{d\mathbf{P}}{dt} = \mathbf{Q} - \mathbf{H}^{\mathsf{T}} \boldsymbol{\Psi}, \\ \mathbf{L} \dfrac{d\boldsymbol{\Psi}}{dt} + \mathbf{R} \boldsymbol{\Psi} = \mathbf{H} \mathbf{P}. \end{cases} \tag{2}$$

In (2),

$$\mathbf{P}(t) := \begin{bmatrix} P_1 & \dots & P_{n_b} & \pi_1 & \dots & \pi_{n_d} & \bar{\pi}_1 & \dots & \bar{\pi}_{n_b} \end{bmatrix}^{\mathsf{T}} \in \mathbb{R}^{n_p}$$

contains the surface pressure $P_1, \dots, P_{n_b}$ at the open boundaries, the set of internal pressure $\pi_1, \dots, \pi_{n_d}$, and the given reference pressures $\bar{\pi}_1, \dots, \bar{\pi}_{n_b}$. Furthermore, the flow rate vector $\mathbf{Q} \in \mathbb{R}^{n_p}$ has the form

$$\mathbf{Q}^{\mathsf{T}} := \begin{bmatrix} Q_1 & \cdots & Q_{n_b} & \underbrace{0 \dots 0}_{n_d + n_b} \end{bmatrix}, \quad Q_k = \int_{\Gamma_k} \boldsymbol{u} \cdot \boldsymbol{n},$$

while $\boldsymbol{\Psi}(t) \in \mathbb{R}^{n_\psi}$ are internal fluxes. The parameters $\mathbf{C} \in \mathbb{R}^{n_p \times n_p}$, $\mathbf{R}, \mathbf{L} \in \mathbb{R}^{n_\psi \times n_\psi}$ denote the symmetric semi-positive capacitance, resistance and inertance matrices of the LPM representing the elastic, viscous and inertial effects, respectively. The matrix $\mathbf{H} \in \mathbb{R}^{n_\psi \times n_p}$ multiplied by $\mathbf{P}$ gives the pressure drops in the different segments of the LPM. A further property of the matrix $\mathbf{H}$ is that, if $\mathbf{C}, \mathbf{R}$ and $\mathbf{L}$ vanish, System (2) reduces to $P_1 = \bar{\pi}, \dots, P_{n_b} = \bar{\pi}_{n_b}$. Hence, Problem (1) with given Neumann data on Γ_{N} can be seen as a particular case of 3D fluid-LPM model. Finally, the system of equations (1)–(2) must be completed with the initial conditions $\boldsymbol{u}(0), \mathbf{P}(0), \boldsymbol{\Psi}(0)$.

Let us now denote with $(\cdot, \cdot)_X$ the usual scalar product in the Sobolev space $L^2(X)$, for an open set $X \subset \mathbb{R}^d$, and let $\| \cdot \|_{0,X}$ be the natural norm associated to the scalar product. Then, the quantities

$$E_\Omega(t) := \frac{\rho}{2} \|\boldsymbol{u}\|_{0,\Omega}^2, \ E_L(t) := \frac{1}{2} \boldsymbol{\Psi}^{\mathsf{T}} \mathbf{L} \boldsymbol{\Psi}, \ E_C(t) := \frac{1}{2} \mathbf{P}^{\mathsf{T}} \mathbf{C} \mathbf{P}, \ D_\Omega(t) := \mu \|\nabla \boldsymbol{u}\|_{0,\Omega}^2, \ D_R(t) := \boldsymbol{\Psi}^{\mathsf{T}} \mathbf{R} \boldsymbol{\Psi}$$

define the kinetic energy of the fluid, the kinetic energy of the LPM, the elastic energy of the LPM, the viscous dissipation of the fluid, and the viscous dissipation of the LPM, respectively.

Using standard arguments, in the non-forced case (i.e. $\boldsymbol{u}_{\mathrm{D}} = \boldsymbol{0}$, $\bar{\pi}_1 = \cdots = \bar{\pi}_{n_b} = 0$) one obtains the following energy balance for the system of equations:

$$\frac{d}{dt}(E_\Omega(t) + E_L(t) + E_C(t)) = -D_\Omega(t) - D_R(t) - \left(\frac{\rho}{2} |\boldsymbol{u}|^2, \boldsymbol{u} \cdot \boldsymbol{n} \right)_{\Gamma_{\mathrm{N}}}. \tag{3}$$

In particular, the last term of the right hand side of (3) might lead to an uncontrolled energy increase during backflow (i.e., when $\boldsymbol{u} \cdot \boldsymbol{n} < 0$ o a subset of Γ_{N}), since this contribution cannot be bounded a priori, if the velocity field at the open boundary is unknown. In practice, backflow instabilities might result in the arise of large unphysical oscillations near the open boundary, which compromise the feasibility and the reliability of the numerical simulations (see the example in Fig. 1).

Remark 1. Let us notice that the stability issues in presence of backflow pointed out in (3) do not depend on the particular formulation of the advection term in the Navier–Stokes equation: for both the convective form $(\mathbf{u} \cdot \nabla)\mathbf{u}$ and the conservative form $\nabla \cdot (\mathbf{u} \otimes \mathbf{u})$, the same boundary term arises, i.e. $\rho/2(|\mathbf{u}|^2, \mathbf{u} \cdot \mathbf{n})$.
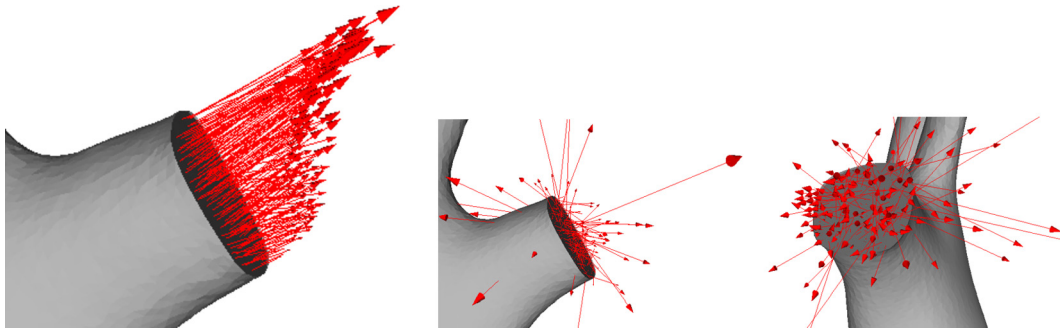
Fig. 1. A typical backflow instability arising in blood flow simulations (at $Re \approx 400$): velocity vectors on the open boundaries at the time of peak outflow (left) and at the time instant when backflow starts at one of the open boundaries (center and right).

1.2. An overview of backflow stabilization strategies

A first class of backflow stabilization methods, which has been discussed in several previous works, is based on modifying the Neumann boundary condition $(1)_5$ as

$$\mu \partial_{\boldsymbol{n}} \boldsymbol{u} - p\boldsymbol{n} = P_k \boldsymbol{n} - \beta \frac{\rho}{2} (\mathbf{f}(\boldsymbol{u}) - \mathbf{g}(\boldsymbol{u}, \boldsymbol{u}_0)) \text{ on } \Gamma_k, \tag{4}$$

where $\beta > 0$ is a parameter, such that $\beta \mathbf{f}(\boldsymbol{u}) \cdot \boldsymbol{u} \geq |\boldsymbol{u}|^2 (\boldsymbol{u} \cdot \boldsymbol{n})$ when $\boldsymbol{u} \cdot \boldsymbol{n} < 0$, and $\boldsymbol{u}_0 : \Gamma_k \to \mathbb{R}^2$ is a given "corrective" boundary velocity profile.

Up to our knowledge, a boundary condition in the form (4) was first introduced in [3,10,11]. In the context of physiological flow simulations, the variant of (4) that is typically employed reads

$$\mathbf{f}(\boldsymbol{u}) = |\boldsymbol{u} \cdot \boldsymbol{n}|^- \boldsymbol{u} , \ \mathbf{g}(\boldsymbol{u}, \boldsymbol{u}_0) = \mathbf{0} , \tag{5}$$

with $|x|^- := (|x| - x)/2$ being the negative part of $x \in \mathbb{R}$. These methods have been widely employed in blood [2,17,29] and respiratory [27,28] flows, and in what follows we will refer to (5) as the *inertial stabilization*. Its main property is that it ensures energy stability if $\beta = 1.0$. Moreover, for $\beta = 1.0$ also the existence of weak solutions can be proven, independently of the viscosity [8].

However, the stabilizing term introduces a boundary condition which is inconsistent with the original problem, even in the relatively simple cases (e.g., a Womersley flow). In fact, the inertial stabilization perturbs the boundary traction in $(1)_5$ in an unphysical way, as it might penalize the velocity entering the domain, hence flattening the boundary velocity profile. The perturbed boundary condition may strongly compromise its accuracy in cases where $P_k \approx \rho |\boldsymbol{u}|^2$. In practice, $\beta < 1.0$ (in order to reduce the boundary perturbation) has often been shown to yield stable results, see, e.g., [17,27].

For the sake of completeness, we mention that a modification of (5) using the smooth function $\Theta(x) = 0.5(1 - \tanh(x/\delta))$ instead of $|x|^-$ was recently proposed in [15,16].

In order to improve the consistency of the inertial stabilization (5), the corrective term

$$\mathbf{g}(\boldsymbol{u}, \boldsymbol{u}_0) = \text{sgn}(|\boldsymbol{u} \cdot \boldsymbol{n}|^-)|\boldsymbol{u}_0 \cdot \boldsymbol{n}|^- \boldsymbol{u}_0 \tag{6}$$

was recently proposed in the context of respiratory flows [22,24]. In particular, the corrective profile $\boldsymbol{u}_0$ was either defined as a parabolic profile of magnitude modulated by a given flow rate, or constructed as a superposition of Womersley modes morphed to the open boundary. The major drawback of this approach is that the computation of the corrective profile typically relies on strong assumptions on the solution (e.g., that the flow is in a periodic regime [24] or that the boundary has a particular shape), or it requires the solution of an additional Stokes problem [11].

All the methods described above are built upon the idea of balancing the convective backflow energy (the last term in (3)) by penalizing the boundary velocity field. An alternative strategy, based on the regularization of the tangential derivatives of the velocity at the open boundary, was recently proposed in [5]. In this case, for each open boundary Γ_k the following stabilization term is introduced in the weak formulation of (1):

$$\mathcal{T}_k(\boldsymbol{u}, \boldsymbol{v}) = \gamma_k \sum_{j=1}^{d-1} \left(|\boldsymbol{u} \cdot \boldsymbol{n}|^- \boldsymbol{t}_j^{\mathsf{T}} \nabla \boldsymbol{u}, \boldsymbol{t}_j^{\mathsf{T}} \nabla \boldsymbol{v} \right)_{\Gamma_k}, \tag{7}$$

where γ_k is a stabilization parameter, the vectors $\boldsymbol{t}_1, \ldots, \boldsymbol{t}_{d-1}$ stand for the tangential directions to Γ_k, and $\boldsymbol{v}$ is a test function. As for the inertial stabilization, the term (7) does not require assumption on the boundary velocity profile and, as shown in [5], the energy stability can be ensured if the parameter γ_k is larger than the Poincaré constant of the domain Γ_k. Similar to the methods outlined above, the stabilization (7) introduces a boundary term which is not consistent with the original problem (1). However, the numerical results showed that the stabilization parameter in (7) can be reduced with

the element mesh size. As a consequence, it was shown that, for the case of a Womersley flow with moderate backflow (in hemodynamic regime), the tangential regularization delivered asymptotically more accurate results than the inertial stabilization [5]. Moreover, it was successfully used for the simulation of venous hemodynamics [12]. Nevertheless, the inconsistency of the stabilization term remained an issue when treating more challenging cases of larger backflow on open boundaries. This situation is typically faced for the simulation of respiratory flows [14,26], where a special interest lies on pressure controlled inflow in mechanical ventilation [35].

For the sake of completeness, it has to be mentioned that other approaches to avoid backflow instabilities have been proposed, based on constraints of the velocity profile on the open boundary. In particular, a first method [25] imposes a given velocity profile (dynamically scaled by the flow rate) through Lagrange multipliers. However, its implementation might result particularly intrusive, and, at the same time, it shifts the local velocity instability issues to the global equilibria of fluxes. A second approach enforces the velocity to be normal to the boundary (see, e.g., [17]) and it is often used in simulation practice, as it can be implemented adding simply a penalization at the weak level. However, in view of (3), it does not guarantee energy stability, as it does not remove the issue of the uncontrolled incoming energy due to the (normal) incoming velocity. Nevertheless, in practice (i.e., at the discrete level), enforcing zero tangential velocity might reduce, or delay, the arise of instabilities, and hence be effective for low backflow regimes. Recently, it was shown in [17] that these two approaches do not deliver satisfactory results in terms of stability and accuracy in hemodynamic relevant regimes.

Finally, in the case of coupled 3D-1D models, a boundary condition which guarantees a stable energy balance on the 3D/1D interface (i.e., the open boundary of the 3D domain) has been recently proposed in [21], based on coupling the total pressures of both bulk (3D) and reduced (1D) models. This approach, however, shifts the issues of spurious incoming energy to the distal open boundary of the 1D domain, so the whole system might still be unstable, and its practical implementation might result particularly intrusive [7].

1.3. Motivation and goals

The aim of this work is to improve the tangential regularization [5], regularizing the numerical solution at the open boundary around a Stokes solution, i.e., the closest stable approximation of Navier–Stokes. Namely, we introduce two additional terms with respect to [5]: the first one takes into account the inertial effects, while the second one mimics a boundary pressure gradients directed normal to each open boundary.

One of the main features of the proposed method, in contrast to the approaches based on (4), is that it is consistent with Womersley flows for arbitrary transients and boundary shapes, without the need of calculating an additional corrective velocity profile. Furthermore, our numerical experiments show that the stabilization parameter can be decreased with the mesh size.

In order to validate the method, we first consider transient three dimensional Womersley flows in relevant physiological regimes (blood and air), monitoring both velocity and pressure profiles against a stable reference solution. In order to demonstrate the importance of the additional terms, we compare our results with the ones obtained with the tangential regularization (7) and with the inertial stabilization (5). As next, we perform numerical simulations for three-dimensional geometries obtained from medical imaging, using physiological input data. It is important to notice that these two flow regimes are characterized by different Reynolds and Womersley numbers, hence making particularly challenging the development of a backflow stabilization suitable for both cases.

The rest of the paper is organized as follows. The stabilized formulation is introduced and analyzed in Section 2. In Section 3 the performance of the method is assessed considering three dimensional transient Womersley flows in blood and air flow regimes, while in Section 4 we present results for real aortic and bronchial geometries. Finally, Section 5 draws the conclusions.

2. The Stokes-residual stabilization

2.1. The stabilized formulation

In order to define the stabilized formulation, we introduce the space

$$H^1_{\mathcal{T}} := \left\{ \boldsymbol{v} \in H^1(\Omega) \mid (\boldsymbol{t}_1^{\mathsf{T}} \nabla \boldsymbol{v})|_{\Gamma_{\mathrm{N}}}, \ldots, (\boldsymbol{t}_{d-1}^{\mathsf{T}} \nabla \boldsymbol{v})|_{\Gamma_{\mathrm{N}}} \in L^2(\Gamma_{\mathrm{N}}) \right\} \subset H^1(\Omega),$$

of the functions whose tangential derivatives are integrable on the open boundary, and the set

$$H^1_{\mathcal{T},0}(\Omega) := \left\{ \boldsymbol{v} \in H^1_{\mathcal{T}}(\Omega) \mid \boldsymbol{v} = \boldsymbol{0} \text{ on } \Gamma_{\mathrm{D}} \cup \Sigma \right\}$$

of the functions in $H^1_{\mathcal{T}}$ which vanish on the Dirichlet boundary. We consider then the following stabilized variational formulation of Problem (1): Find $\boldsymbol{u}(t) \in H^1_{\mathcal{T}}(\Omega)$ satisfying the Dirichlet boundary conditions (1)$_{3-4}$, $p(t) \in L^2(\Omega)$, $\mathbf{P}(t) \in \mathbb{R}^{n_p}$, and $\Psi(t) \in \mathbb{R}^{n_\psi}$, such that, for all $0 < t \leq T$,

$$\begin{cases} \mathcal{A}(\boldsymbol{u}, \boldsymbol{v}) + \displaystyle\sum_{k=1}^{n_b} \mathcal{S}_k(\boldsymbol{u}, \boldsymbol{v}) - \mathcal{B}(p, \boldsymbol{v}) = - \displaystyle\sum_{k=1}^{n_b} (P_k \boldsymbol{n}, \boldsymbol{v})_{\Gamma_k}, \\[2mm] \qquad\qquad \mathcal{B}(q, \boldsymbol{u}) = 0, \\[2mm] \qquad\qquad \mathbf{C}\dfrac{d\mathbf{P}}{dt} = \mathbf{Q} - \mathbf{H}^{\mathsf{T}}\boldsymbol{\Psi}, \\[2mm] \qquad\qquad \mathbf{L}\dfrac{d\boldsymbol{\Psi}}{dt} + \mathbf{R}\boldsymbol{\Psi} = \mathbf{H}\mathbf{P} \end{cases} \tag{8}$$

for all $\boldsymbol{v} \in H^1_{\mathcal{T},0}(\Omega)$ and $q \in L^2(\Omega)$. In (8), the classical bilinear forms are defined by

$$\mathcal{A}(\boldsymbol{u}, \boldsymbol{v}) := \rho\,(\partial_t \boldsymbol{u}, \boldsymbol{v})_\Omega + \rho\,(\boldsymbol{u} \cdot \nabla \boldsymbol{u}, \boldsymbol{v})_\Omega + \mu\,(\nabla \boldsymbol{u}, \nabla \boldsymbol{v})_\Omega + \frac{\rho}{2}\,(\nabla \cdot \boldsymbol{u}, \boldsymbol{v} \cdot \boldsymbol{u})_\Omega,$$
$$\mathcal{B}(p, \boldsymbol{v}) := (p, \nabla \cdot \boldsymbol{v})_\Omega. \tag{9}$$

where the last term in $(9)_1$ is the so-called Temam stabilization [33], used for improving the energy balance at the space-semidiscrete level, since the divergence-free condition holds in general only in a weak sense. Note that using the conservative form of the advection term, the Temam term to be included has the same form, but with opposite sign.

Finally, the stabilization term $\mathcal{S}_k(\boldsymbol{u}, \boldsymbol{v})$ is defined considering the weak residual of a Stokes problem at the open boundary Γ_k, driven by a given pressure gradient normal to the boundary:

$$\mathcal{S}_k(\boldsymbol{u}, \boldsymbol{v}) := \ell_k^{\mathrm{e}} \left(\int_{\Gamma_k} (\rho\,\partial_t \boldsymbol{u} + a_k(t)\boldsymbol{n}) \cdot \boldsymbol{v} + \mu\mathcal{V}(\boldsymbol{u}, \boldsymbol{v}) \right). \tag{10}$$

In (10) the viscous term is defined by

$$\mathcal{V}(\boldsymbol{u}, \boldsymbol{v}) := \sum_{j=1}^{d-1}\left((\boldsymbol{t}_j^{\mathsf{T}}\nabla(\boldsymbol{v} \cdot \boldsymbol{n}))^{\mathsf{T}}\left(\boldsymbol{t}_j^{\mathsf{T}}\nabla(\boldsymbol{u} \cdot \boldsymbol{n})\right) + \sum_{i=1}^{d-1}(\boldsymbol{t}_j^{\mathsf{T}}\nabla(\boldsymbol{v} \cdot \boldsymbol{t}_i))^{\mathsf{T}}\left(\boldsymbol{t}_j^{\mathsf{T}}\nabla(\boldsymbol{u} \cdot \boldsymbol{t}_i)\right) \right), \tag{11}$$

$\ell_k^{\mathrm{e}} \geq 0$ denotes a stabilization parameter and $a_k(t)$ is an approximation of the *open boundary pressure gradient*, whose computation will be discussed in detail in the next Section 2.2.

Note that choosing $\ell_k^{\mathrm{e}} = 0$ (for $k = 1, \ldots, n_b$) we retrieve the variational formulation of the original Problem, up to the Temam term. In practice, as it will be shown in Section 2.3, the stabilization parameter ℓ_k^{e} can be defined according to the physical parameters of the problem. In particular, taking $\ell_k^{\mathrm{e}} \neq 0$ only in presence of backflow on the boundary Γ_k yields a variational form consistent with the original Problem during outflow, as for the other approaches reviewed in Section 1.2.

Remark 2. It is worth mentioning that the definition of the stabilization term (10) does not depend on the (symmetric or non-symmetric) formulation of the strain rate tensor used in the bulk domain. In particular, the numerical examples that we will shown in Sections 3 and 4 are based on the non-symmetric formulation. However, in our experience we did not observe any substantial differences in terms of arise of instabilities nor in the performance of the stabilization methods, when using the symmetric formulation.

2.2. Approximation of the open boundary pressure gradient

In practice, a key issue for the definition of the stabilized formulation (8) is the choice of the pressure gradient $a_k(t)$ on the open boundary Γ_k. In the general case, this function is not available a priori, and it has to be approximated from the numerical solution. To this aim, we propose to use a simple lumped parameter model

$$a_k(t) = -L_k \dot{Q}_k(t) - r_k Q_k(t) \tag{12}$$

in order to relate the sought pressure gradient on Γ_k with the flow rate $Q_k = \int_{\Gamma_k} \boldsymbol{u}(\mathbf{x}, t) \cdot \boldsymbol{n}$.

In order to define the parameters L_k and r_k, let us first consider the case of a unidirectional Stokes flow, i.e., with a velocity profile $\boldsymbol{u}(\mathbf{x}, t) = U_k(\mathbf{x}, t)\boldsymbol{n}$ normal to the open boundary, and satisfying the equation

$$\rho\,\partial_t U_k + \mu \Delta U_k + a_k = 0 \tag{13}$$

Integrating (13) over Γ_k, and comparing the result with (12) yield

$$L_k = \frac{\rho}{|\Gamma_k|},$$

$$r_k = \frac{\mu}{|\Gamma_k|} \int_{\Gamma_k} \Delta \bar{U}_k = \frac{\mu}{|\Gamma_k|} \oint_{\partial \Gamma_k} \nabla \bar{U}_k \cdot \boldsymbol{v}_k \tag{14}$$

where $\overline{U}_k$ stands for a renormalized velocity profile (i.e. having a unitary integral on Γ_k), and $\boldsymbol{v}_k$ is the normal to $\partial \Gamma_k$ pointing outwards Γ_k.

In view of $(14)_2$, we then consider two possible approaches for computing the resistance r_k in general cases:

1. the **Poiseuille** approximation, given by the resistance of a unitary profile $\overline{U}_k(t)$ of parabolic shape:

$$r_k = r_k^{\text{pois}} := \begin{cases} \dfrac{12\mu}{|\Gamma_k|^3}, & \text{for } d = 2, \\ \dfrac{8\mu\pi}{|\Gamma_k|^2} & \text{for } d = 3. \end{cases} \tag{15}$$

2. the **dynamic** approximation, using $(14)_2$ in a time-discrete setting, and choosing $U_k(t)$ as the solution $\boldsymbol{u}_n$ at the previous time step:

$$r_k = r_k^{\text{dyn}} := \begin{cases} \dfrac{\mu}{|\Gamma_k| Q_k^n} \oint_{\partial \Gamma_k} \nabla (\boldsymbol{u}_n \cdot \boldsymbol{n}) \cdot \boldsymbol{v}_k, & \text{if } Q_k^n \neq 0 \\ 0, & \text{if } Q_k^n = 0 \end{cases} \tag{16}$$

with $Q_k^n = \int_{\Gamma_k} \boldsymbol{u}_n \cdot \boldsymbol{n}$.

It is worth noticing that in order to define the resistance as in (16) at the continuous level, one has to restrict the solution space to the functions whose normal derivative is integrable along $\partial \Gamma_k$. However, this additional assumption is not strictly required for defining the Stokes-residual (10) on the boundary, as the function $a_k(t)$ could be either a given function of time, or computed through (12) with values of r_k and L_k depending only on physical and geometrical parameters (e.g., using the Poiseuille approximation of the resistance (15)).

Furthermore, in the numerical tests considered in this work, the flow rate and its time derivative in expression (12) have been approximated explicitly using the solution at two previous time steps, i.e.

$$Q_k = Q_k^n = \int_{\Gamma_k} \boldsymbol{u}_n \cdot \boldsymbol{n} \quad, \quad \dot{Q}_k = \frac{1}{\tau} \int_{\Gamma_k} (\boldsymbol{u}_n - \boldsymbol{u}_{n-1}) \cdot \boldsymbol{n} \tag{17}$$

where n and $n-1$ indicate the indices of the last two time steps, and τ stands for the time step size.

2.3. Energy-based time-stability analysis

As a preliminary step, let us define

$$E_e(t) := \frac{\rho}{2} \sum_{k=1}^{n_b} \frac{\ell_k^e}{|\Gamma_k|} \left\{ |\Gamma_k| \int_{\Gamma_k} |\boldsymbol{u}(t)|^2 - Q_k^2(t) \right\}.$$

Applying Cauchy–Schwarz to the flux integral, one obtains

$$Q_k^2(t) = \left(\int_{\Gamma_k} \boldsymbol{u}(t) \cdot \boldsymbol{n} \right)^2 \leq \left(\int_{\Gamma_k} |\boldsymbol{u}(t)|^2 \right) \left(\int_{\Gamma_k} |\boldsymbol{n}|^2 \right) = |\Gamma_k| \int_{\Gamma_k} \boldsymbol{u}(t)^2$$

which implies $E_e(t) \geq 0$. Then, we can derive the following energy inequality for the stabilized formulation.

Proposition 1. *Let $\boldsymbol{u}(t)$, $\boldsymbol{\Psi}(t)$ and $\mathbf{P}(t)$ be the solution of Problem (8) in the case of an unforced system (i.e., $\boldsymbol{u}_D = \mathbf{0}$, $\bar{\pi}_1 = \cdots = \bar{\pi}_{n_b} = 0$). Then, there exists a set of parameters $\ell_1^e, \ldots, \ell_{n_b}^e$ (large enough) so that the following energy inequality holds*

$$\frac{\mathrm{d}}{\mathrm{d}t} \left(E_\Omega(t) + E_L(t) + E_C(t) + E_e(t) \right) \leq -D_\Omega(t) - D_R(t) + \sum_{k=1}^{n_b} \ell_k^e r_k Q_k^2(t). \tag{18}$$

Proof. Testing Equations (8)$_{1-2}$ with $\boldsymbol{v} = \boldsymbol{u}$ and $q = p$, and by pre-multiplying (8)$_3$ and (8)$_4$ by $\mathbf{P}^\mathsf{T}$ and $\boldsymbol{\Psi}^\mathsf{T}$, respectively, one obtains

$$\frac{\mathrm{d}}{\mathrm{d}t}\left(E_\Omega(t) + E_L(t) + E_C(t) + E_\mathrm{e}(t)\right)$$

$$= -D_\Omega(t) - D_R(t) + \sum_{k=1}^{n_b} \ell_k^\mathrm{e} r_k Q_k^2(t)$$

$$- \frac{\rho}{2} \int_\Omega \boldsymbol{u} \cdot \nabla |\boldsymbol{u}|^2 - \frac{\rho}{2}\left(\nabla \cdot \boldsymbol{u}, |\boldsymbol{u}|^2\right)_\Omega - \sum_{k=1}^{n_b} \ell_k^\mathrm{e}\mu \int_{\Gamma_k} \mathcal{V}(\boldsymbol{u}, \boldsymbol{u})$$

$$= -D_\Omega(t) - D_R(t) + \sum_{k=1}^{n_b} \ell_k^\mathrm{e} r_k Q_k^2(t) - \frac{\rho}{2}\sum_{k=1}^{n_b} \underbrace{\left(\int_{\Gamma_k} |\boldsymbol{u}|^2 (\boldsymbol{u} \cdot \boldsymbol{n}) + \frac{2\mu}{\rho}\ell_k^\mathrm{e} \int_{\Gamma_k} \mathcal{V}(\boldsymbol{u}, \boldsymbol{u})\right)}_{I_k}.$$

In the case $\boldsymbol{u} \cdot \boldsymbol{n} \geq 0$ on Γ_k (outflow) it holds $I_k > 0$, which implies (18). In the case of $\boldsymbol{u} \cdot \boldsymbol{n} < 0$ (backflow) on a subset $\Gamma_{k,b} \subseteq \Gamma_k$, one can write

$$I_k = \underbrace{\int_{\Gamma_k \backslash \Gamma_{k,b}} |\boldsymbol{u}|^2 (\boldsymbol{u} \cdot \boldsymbol{n})}_{>0} - \int_{\Gamma_{k,b}} |\boldsymbol{u}|^2 |\boldsymbol{u} \cdot \boldsymbol{n}| + \frac{2\mu}{\rho}\ell_k^\mathrm{e} \int_{\Gamma_k} \mathcal{V}(\boldsymbol{u}, \boldsymbol{u})$$

which, since $\mathcal{V}(\boldsymbol{u}, \boldsymbol{u}) > 0$, yields

$$I_k \geq -\int_{\Gamma_{k,b}} |\boldsymbol{u}|^2 |\boldsymbol{u} \cdot \boldsymbol{n}| + \frac{2\mu}{\rho}\ell_k^\mathrm{e} \int_{\Gamma_{k,b}} \mathcal{V}(\boldsymbol{u}, \boldsymbol{u})$$

$$> -U_b^{(k)} \int_{\Gamma_{k,b}} |\boldsymbol{u}|^2 + \frac{2\mu}{\rho}\ell_k^\mathrm{e} \int_{\Gamma_{k,b}} \mathcal{V}(\boldsymbol{u}, \boldsymbol{u}), \tag{19}$$

where

$$U_b^{(k)} \geq \max_{\boldsymbol{x} \in \Gamma_{k,b}(t)}(|\boldsymbol{u}(\boldsymbol{x}, t) \cdot \boldsymbol{n}|)$$

is an upper bound for the backflow velocity.

If we then choose the stabilization parameter ℓ_k^e in the form

$$\ell_k^\mathrm{e} = \frac{\rho \sigma_k U_b^{(k)}}{2\mu}, \tag{20}$$

(with $\sigma_k > 0$), we can rewrite (19) as

$$I_k > \frac{U_b^{(k)}\rho}{2\mu}\left(-\int_{\Gamma_{k,b}} |\boldsymbol{u}|^2 + \sigma_k \int_{\Gamma_{k,b}} \mathcal{V}(\boldsymbol{u}, \boldsymbol{u})\right). \tag{21}$$

Hence, taking σ_k equal to the Poincaré's constant of the domain Γ_k, the following relation holds

$$\int_{\Gamma_{k,b}} |\boldsymbol{u}|^2 = \int_{\Gamma_{k,b}} (\boldsymbol{u} \cdot \boldsymbol{n})^2 + \int_{\Gamma_{k,b}} (\boldsymbol{u} \cdot \boldsymbol{t}_i)^2$$

$$< \sigma_k \sum_{j=1}^{d-1} \int_{\Gamma_{k,b}} |\boldsymbol{t}_j^\mathsf{T} \nabla(\boldsymbol{u} \cdot \boldsymbol{n})|^2 + \sigma_k \sum_{j,i=1}^{d-1} \int_{\Gamma_{k,b}} |\boldsymbol{t}_j^\mathsf{T} \nabla(\boldsymbol{u} \cdot \boldsymbol{t}_i)|^2, \tag{22}$$

which substituted into (21) yields $I_k > 0$. $\square$

The above proof (Equation (20)) suggests also a possible choice of ℓ_k^e as a function of the material constants ρ and μ, of an upper bound for the backflow velocity, and of the Poincaré constant σ_k of the open boundary Γ_k. In the numerical results presented in the next sections, the stabilization parameter will be defined as a function of the backflow velocity. However, numerical evidence showed that σ_k depends on the discretization, and that it can be reduced with the mesh characteristic size, similarly to what was observed for the stabilization method proposed in [5].

In general, Proposition 1 states only the conditional stability of the formulation (8) in general. However, in several situations of practical interests, a stable energy balance can be assured:

Corollary 1. *The non-forced solution $\boldsymbol{u}(t)$, $\mathbf{P}(t)$, $\boldsymbol{\Psi}(t)$ of Problem (8) is stable in the sense of Lyapunov if one of the following conditions is fulfilled:*

1. *There is only one open boundary ($n_b = 1$). In fact, in this case global mass conservation implies $Q_1(t) = 0$.*
2. *The physical LPM (2) used for computing the Neumann data on the open boundary boundaries is such that*

$$D_R(t) \geq \sum_{k=1}^{n_b} \ell_k^e r_k Q_k^2(t). \tag{23}$$

In other words, energy stability holds if the physical LPM is more dissipative than the LPM (12) used for computing the pressure gradient $a_k(t)$.

In practice, a sufficient condition for satisfying inequality (23) is that the physical resistance proximal to each open boundary Γ_k is larger to the resistance of the backflow stabilization term $\ell_k^e r_k$. In the numerical examples, we will verify the fulfillment of (23) according to this criterion. Notice that, using the Poiseuille approximation (15) for the resistance r_k, the stability condition (23) can be verified a priori, if a bound on the backflow velocity is available (using (20)).

3. Numerical experiments for Womersley flows

In this section we assess the performance of the Stokes-residual based stabilization for blood flows through different numerical tests based on a transient Womersley flow.

The Womersley solution describes a flow in a pipe driven by an oscillating pressure gradient, and it is very popular in physiological flow simulations. In particular, it has already been used to benchmark stabilization methods in [22,24], where, however, only results in terms of mean flow rates and pressures were reported. Hereafter, we compare the stabilized solution for velocity and pressure against a stable reference solution. To the authors best knowledge, such detailed comparison with a reference solution (as the one discussed in Sections 3.2–3.3) has not been presented yet for other backflow stabilization methods.

3.1. Numerical method

For all examples reported in this work, the numerical solutions were computed using a non-incremental Chorin–Temam pressure projection method [13,23,33], treating the time derivative of the velocity with a backward Euler method, and treating explicitly the advective velocity in the convection term. Stabilized $\mathbb{P}_1/\mathbb{P}_1$ finite elements have been used for the spatial discretization, together with an SUPG stabilization for the convection [9] (the SUPG-factor was set as small as possible so that the simulation still remains stable during outflow).

For the time discretization of the stabilization term (10), we treat implicitly the linear inertial and viscous terms, while the open boundary pressure gradient is computed explicitly approximating the flow rate with (17), in order to avoid a non-local coupling of the degrees of freedom at the open boundaries.

Furthermore, in view of the proof of Proposition 1 (Equation (20)), we compute explicitly the parameter ℓ_k^e at time step $n + 1$, proportional to the maximum backflow velocity on Γ_k at time step n:

$$\ell_k^e = \frac{\rho \sigma U_{b,n}^{(k)}}{2\mu}, \tag{24}$$

with

$$U_{b,n}^{(k)} = \max_{\boldsymbol{x} \in \Gamma_k}(|\boldsymbol{u}_n(\boldsymbol{x}) \cdot \boldsymbol{n}|^-).$$

In all cases, the parameter σ has been chosen as small as possible so that the simulation remained stable during backflow, and equal for all open boundaries. Note that doing so, the stabilization term is only active during backflow, as for the inertial stabilization and tangential regularization methods.

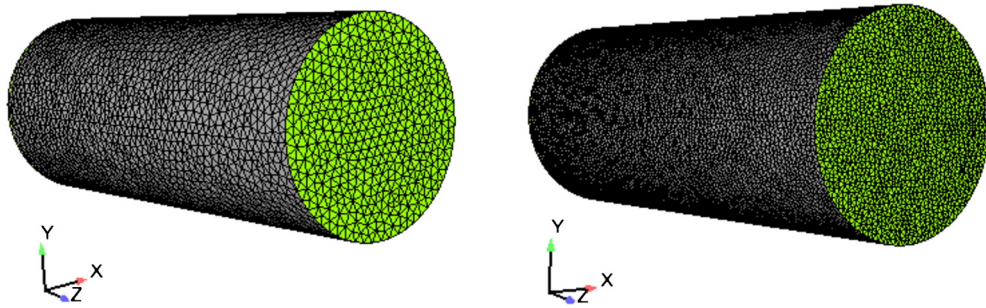In what follows, all quantities are expressed in CGS units.

Fig. 2. The coarse (left) and fine (right) meshes used for the Womersley testcases.

3.2. Blood flow regime

We consider an incompressible flow in a cylindrical domain of radius $R = 1$ and length $B = 5$, driven by an oscillating pressure drop of amplitude $\delta p = 2000$ and frequency $\omega = 2\pi$. The physical properties of the fluid are taken as $\rho = 1.0$ and $\mu = 0.035$, corresponding to typical values for blood flows in large arteries, resulting in a Womersley number of $\alpha = R\sqrt{\omega\rho/\mu} = 13.3$.

For the numerical tests, the domain has been discretized with two mesh characteristic sizes: $h = 0.12$ (*coarse*) and $h = 0.06$ (*fine*), see Fig. 2.

The simulations for the Navier–Stokes problem were setup as follows. First, a numerical solution was computed solving a Stokes equation (validated against the periodic analytical solution, see, e.g., [19]), with a given pressure gradient $(\delta p/B) \sin \omega t$ between Γ_D ($z = 0$) and $\Gamma_N = \Gamma_1$ ($z = B$). The resulting inlet transient velocity profile between $t = 0$ s and $t = 1.0$ s was then used in the Navier–Stokes simulations as a Dirichlet boundary condition on Γ_D, while a homogeneous pressure was enforced at the open boundary Γ_N. In this configuration, the Reynolds number during backflow reaches the value $Re = 1000$. We employed a uniform time-step of size $5 \cdot 10^{-4}$.

Notice that since the velocity profile does not vary along the z-direction, there is no physical convection and thus the analytical solutions for Stokes and Navier–Stokes problems coincide. Nevertheless, due to the numerical approximations (e.g. weak incompressibility of the solution, mesh asymmetries, linear solver, etc.) spurious convective effects are introduced in the non-linear case, and without any stabilization the Navier–Stokes solution becomes unstable during backflow. However, a stable reference solution can be computed solving a Stokes problem on the same geometry, which can be then used to assess the accuracy of the stabilized Navier–Stokes formulation.

The results of the stabilized formulation are shown in Figs. 3 (coarse mesh) and 4 (fine mesh). In particular, we compare the velocity profile at the open boundary and the pressure along the centerline obtained with the stabilized Navier–Stokes solution with the reference Stokes solution. Besides the results of the two different versions of the Stokes-residual stabilization (Figs. 3–4, top), also the results of the inertial stabilization and tangential regularization (in both cases selecting the respective stabilization parameter as small as possible) are shown (Figs. 3–4, bottom).

From these results, one can conclude that the Stokes-residual stabilization outperforms both the inertial stabilization and the tangential regularization concerning the outlet velocity profile (Figs. 3–4, left). While the inertial stabilization tends to flatten the profile and for the tangential regularization the boundary profile gets close to a parabola, the Stokes-residual stabilized solution has a shape much similar to the reference Stokes solution. Concerning the pressure (Figs. 3–4, right), the Stokes-residual stabilization yields peak errors of about 5% (dynamical resistance (16)) and 12% (Poiseuille resistance (15)), which decrease to 4% and 9%, respectively, refining the mesh. The tangential regularization has a comparable performance for the coarse and fine meshes (peak pressure error 8%). In both cases, the inertial stabilization has the largest pressure errors, with peaks close to 18%.

Finally, Fig. 5 shows the boundary pressure gradients approximated using the lumped parameter model (12), with the Poiseuille (15) and the dynamic (16) resistance approximations. The curves are compared with the analytical profile, showing that both approaches achieve a very good agreement with the analytical curve, and that the precision improves on the finer mesh. In particular, the dynamic approximation appears slightly more accurate, especially during backflow (starting from 0.8 s), consistently with what is observed in Figs. 3–4.

It is important to observe that, using a finer mesh, we were able to decrease the stabilization parameter (from $\sigma = 0.002$ to $\sigma = 0.0005$). This phenomenon was already observed in [5], where it was also shown that, in a simplified setting, the spurious frequencies of the discrete solution can be controlled by the viscous part of the stabilization choosing the parameter as $\mathcal{O}(h^2)$.

3.3. Respiratory flow regime

In this section we deal with a transient Womersley flow relevant to respiratory physiology, setting the physical constants equal to $\rho = 0.0011176$, $\mu = 0.000186$, $\delta p = 2.526$, $\omega = 0.5\pi$ (Womersley number $\alpha = 3.0$). In this configuration, the
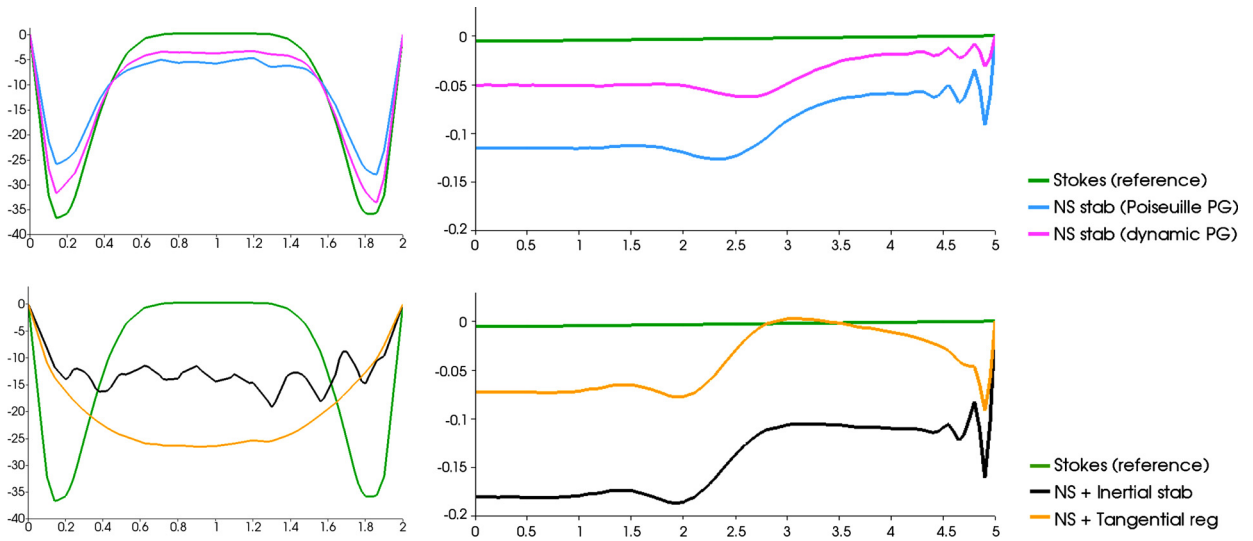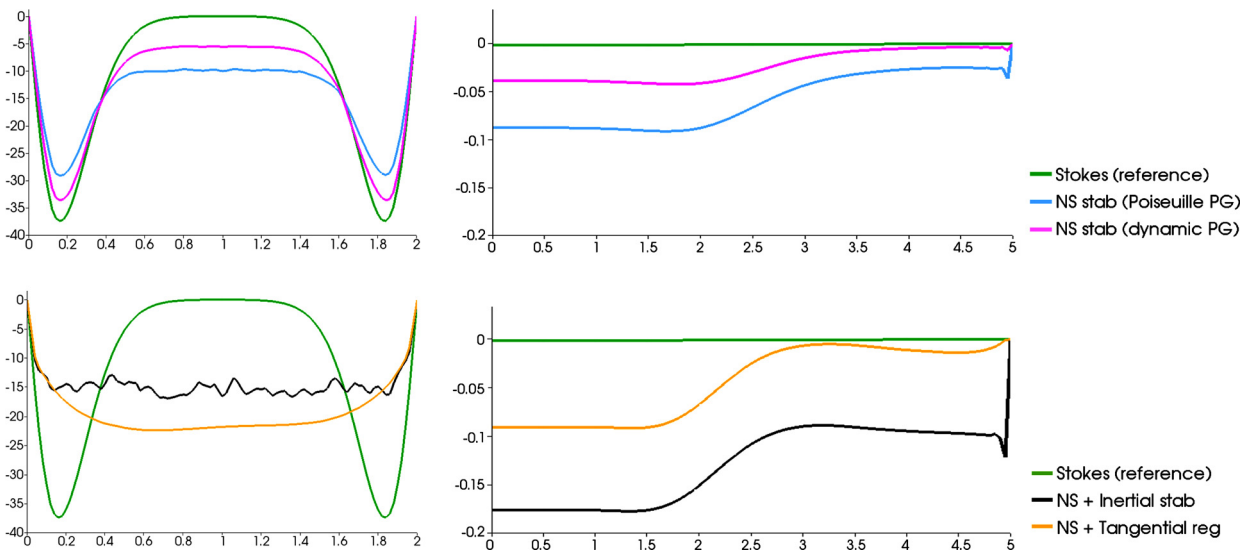
Fig. 3. Results of the 3D-Womersley flow (blood regime) with the coarse mesh size ($h = 0.12$): normal component of the velocity on a longitudinal cut of the outlet boundary (left) and pressure along the centerline $x = y = 0$ normalized by δp (right) at the time instant of peak backflow ($t = 1.0$ s). Top: comparisons of the reference Stokes solution (green) and the Navier–Stokes solutions obtained with the Stokes-residual stabilization ($\sigma = 0.002$), with the two proposed approximations of the boundary pressure gradient (cyan: Poiseuille resistance approximation (15); magenta: dynamic resistance approximation (16)). Bottom: comparisons of the reference Stokes solution (green) with the inertial stabilization with $\beta = 0.6$ (black) and of the tangential regularization with $\gamma = 0.01$ (orange). (For interpretation of the references to color in this figure legend, the reader is referred to the web version of this article.)

Fig. 4. Results of the 3D-Womersley flow (blood regime) with the fine mesh size ($h = 0.06$): normal component of the velocity on a longitudinal cut of the outlet boundary (left) and pressure along the centerline $x = y = 0$ normalized by δp (right) at the time instant of peak backflow ($t = 1.0$ s). Top: comparisons of the reference Stokes solution (green) and the Navier–Stokes solutions obtained with the Stokes-residual stabilization ($\sigma = 0.0005$), with the two proposed approximations of the boundary pressure gradient (cyan: Poiseuille resistance approximation (15); magenta: dynamic resistance approximation (16)). Bottom: comparisons of the reference Stokes solution (green) with the inertial stabilization with $\beta = 0.4$ (black) and of the tangential regularization with $\gamma = 0.005$ (orange). (For interpretation of the references to color in this figure legend, the reader is referred to the web version of this article.)

Reynolds number at peak backflow reaches Re = 2100. The geometry and the numerical scheme are the same as for the blood flow benchmark, but for the current case we employ a time step equal to 10^{-3}.

The velocity and the pressure profiles are shown in Figs. 6–7, confirming the findings of Section 3.2. Firstly, the numerical solutions with the different variants of the Stokes-residual stabilization remain stable also during backflow. Secondly, the solution obtained using the dynamic resistance lies closer to the reference Stokes solution than the one obtained with the Poiseuille resistance. Finally, the stabilization parameter σ can be reduced with the mesh size h, which also allows to obtain a more accurate solution with the fine mesh.
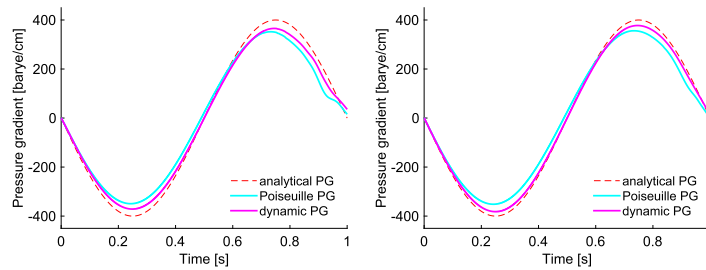
Fig. 5. Comparison of the different approximations for the open boundary pressure gradients $a(t)$ to be used for the Stokes-residual stabilization for the 3D-Womersley blood flow: Poiseuille pressure gradient (cyan); dynamic pressure gradient (magenta). For reference, the analytical pressure gradient is also shown (dashed red). Left: coarse mesh ($h = 0.12$). Right: fine mesh ($h = 0.06$). (For interpretation of the references to color in this figure legend, the reader is referred to the web version of this article.)
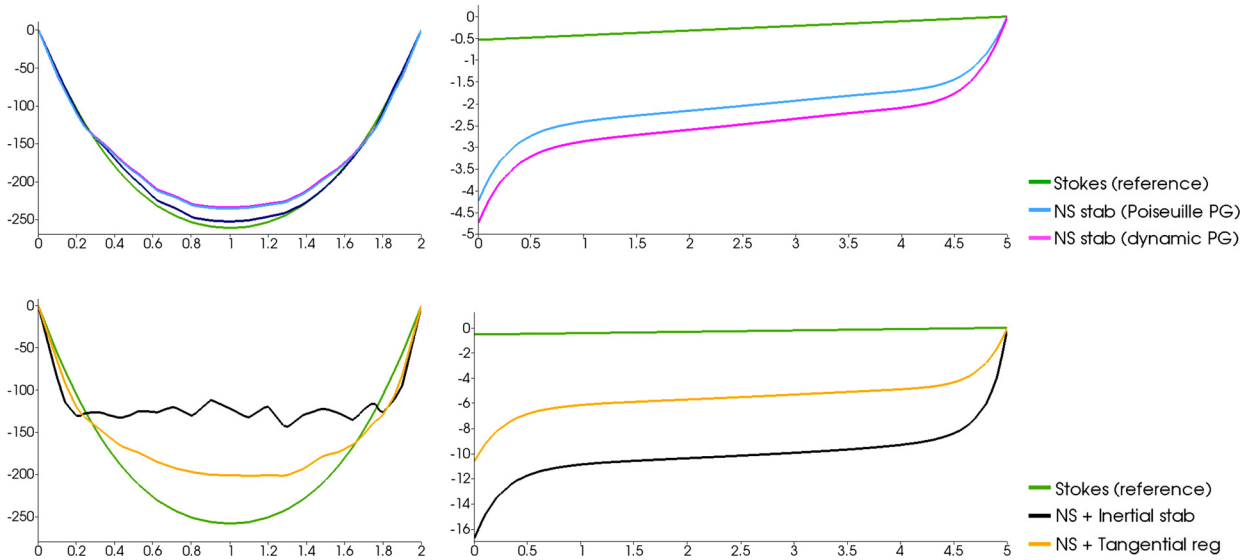
Fig. 6. Results of the 3D Womersley flow (air regime) with the coarse mesh size ($h = 0.12$): normal component of the velocity on a longitudinal cut of the outlet boundary (left) and pressure along the centerline $x = y = 0$ normalized by δp on $z = 0$ (right) at the time instant of peak backflow ($t = 3.6$ s). Top: comparisons of the reference Stokes solution (green) and the Navier–Stokes solutions obtained with the Stokes-residual stabilization ($\sigma = 0.002$), with the two proposed approximations of the boundary pressure gradient (cyan: Poiseuille resistance approximation (15); magenta: dynamic resistance approximation (16)). Bottom: comparisons of the reference Stokes solution (green) with the inertial stabilization with $\beta = 0.5$ (black) and of the tangential regularization with $\gamma = 0.005$ (orange). (For interpretation of the references to color in this figure legend, the reader is referred to the web version of this article.)

In the air flow regime, the Stokes-residual stabilization (Figs. 6–7, top) largely outperforms both inertial stabilization and tangential regularization (Figs. 6–7, bottom), for both velocity and pressure. In fact, the results for the velocity confirm that the inertial stabilization tends to flatten the boundary profile, while the tangential regularization achieves a more paraboloid shape, which, in the particular case of respiratory flow, is closer to the reference solution. For all methods, although the approximation of the velocity fields have an accuracy comparable with the blood flow case, the errors in pressure resulted larger than in blood flows.

However, the Stokes-residual stabilizations deliver a pressure profile considerably closer to the reference solution than the other stabilizations. Moreover, the accuracy of the Stokes-residual stabilizations drastically improves refining the mesh, especially using the dynamic resistance approximation, while the errors of the tangential regularization and inertial stabilization remain of the same order.

Finally, Fig. 8 shows the boundary pressure gradients approximated using the lumped parameter model (12), with the Poiseuille (15) and the dynamic (16) resistance approximations. The curves are compared with the analytical profile, showing that the dynamic approximation achieves a very good agreement with the analytical curve both in outflow and in backflow (between 2.5 s and 4 s), outperforming the Poiseuille approximation. Moreover, the precision improves on the finer mesh. These results are consistent with the accuracy of velocity and pressure (Figs. 6–7).

4. Patient-specific testcases

As next, we assess the performance of the Stokes-residual stabilization for the simulation of blood and respiratory flow in complex geometries obtained from medical imaging. In these cases, a reference stable solution is not available. Hence,
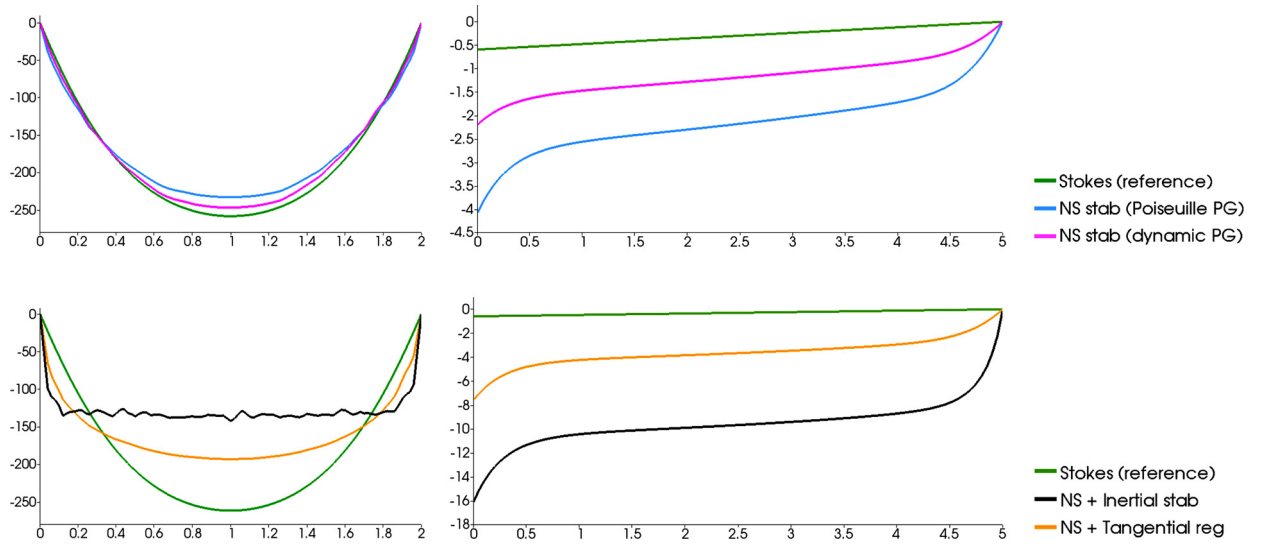
Fig. 7. Results of the 3D Womersley flow (air regime) with the fine mesh size ($h = 0.06$): normal component of the velocity on a longitudinal cut of the outlet boundary (left) and pressure along the centerline $x = y = 0$ normalized by δp (right) at the time instant of peak backflow ($t = 3.6$ s). Top: comparisons of the reference Stokes solution (green) and the Navier–Stokes solutions obtained with the Stokes-residual stabilization ($\sigma = 0.0005$), with the two proposed approximations of the boundary pressure gradient (cyan: Poiseuille resistance approximation (15); magenta: dynamic resistance approximation (16)). Bottom: comparisons of the reference Stokes solution (green) with the inertial stabilization with $\beta = 0.2$ (black) and of the tangential regularization with $\gamma = 0.0005$ (orange). (For interpretation of the references to color in this figure legend, the reader is referred to the web version of this article.)
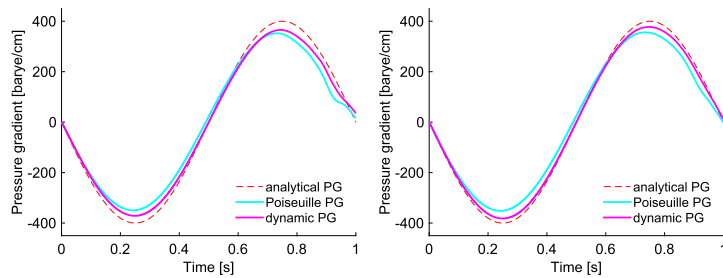
Fig. 8. Comparison of the different approximations for the open boundary pressure gradients $a(t)$ to be used for the Stokes-residual stabilization for the 3D-Womersley air flow: Poiseuille pressure gradient (cyan); dynamic pressure gradient (magenta). For reference, the analytical pressure gradient is also shown (dashed red). Left: coarse mesh ($h = 0.12$). Right: fine mesh ($h = 0.06$). (For interpretation of the references to color in this figure legend, the reader is referred to the web version of this article.)

the goal of these examples is to confirm the robustness of the proposed stabilization method also in more challenging and relevant situations.

4.1. Blood flow in the ascending aorta

The first example consists in the simulation of the blood flow in a patient-specific aorta, obtained from the euHeart database (www.euheart.eu), see Fig. 9. The geometry was segmented from medical images using a segment growing registration algorithm [1], and the finite element mesh was generated on a cut of the original geometry using 3-matic (Materialise, Leuven, Belgium) and TetGen [32]. For the numerical simulations, we considered two different level of refinement for the computational mesh (Fig. 9), denoted in what follows as *coarse* (characteristic element size $h_{\max} = 0.11$) and *fine* (characteristic element size $h_{\max} = 0.055$).

At the inlet boundary (ascending aorta), we impose a plug flow profile with amplitude based on the phase contrast MRI measured flow rate from the same patient (peak flow rate of 350), with a Reynolds number at peak backflow of $Re = \rho U_{\mathrm{mean}}(2R)/\mu \approx 200$. At each open boundary Γ_k, three-elements Windkessel models were used to represent the effect of the neglected downstream circulation, i.e.

$$\mathbf{C}_k = \begin{bmatrix} 0 & 0 \\ 0 & C_k^d \end{bmatrix}, \quad \mathbf{L}_k = \begin{bmatrix} 0 & 0 \\ 0 & 0 \end{bmatrix}, \quad \mathbf{R}_k = \begin{bmatrix} R_k^p & 0 \\ 0 & R_k^d \end{bmatrix}, \quad \mathbf{H}_k = \begin{bmatrix} 1 & -1 \\ 0 & 1 \end{bmatrix}.$$
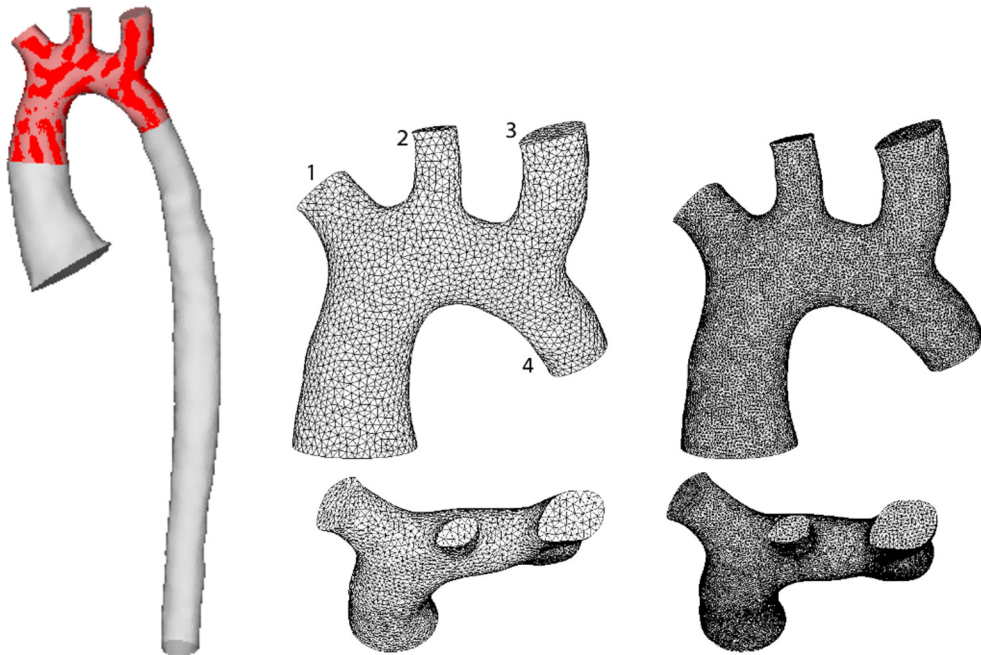
Fig. 9. Left: original patient-specific aortic geometry (grey) and the computational geometry (red). Frontal and top views of the coarse (center) and fine (right) meshes used in the numerical simulations. The open boundaries (1 to 4) are numbered according to the initial direction of the flow. (For interpretation of the references to color in this figure legend, the reader is referred to the web version of this article.)

Table 1
The parameters of the three-elements Windkessel models for the ascending aorta (first to third row), and the maximum values over time of the resistances due to the stabilization term (for the coarse mesh), using the Poiseuille and dynamics approximations (fourth and fifth row, respectively).

	Γ_1	Γ_2	Γ_3	Γ_4
R^p [g/(s cm^4)]	250	683	615	94
R^d [g/(s cm^4)]	10 000	12 960	11 664	1794
C^d [s^2 cm^4/g]	0.0004	0.0002	0.0002	0.0014
$\max_t\{\ell_k^e\, r_k^{pois}\}$ [s^2 cm^4/g]	3.9	32.1	4.8	0.45
$\max_t\{\ell_k^e\, r_k^{dyn}\}$ [s^2 cm^4/g]	6.75	39.2	9.8	0.62

The values of the parameters $R_k^p, R_k^d, C_k^d > 0$ at each open boundary, detailed in Table 1, were calibrated in order to approximate the available measured pressures and the measured flows [4]. The time-coupling of the Windkessel models and the 3D fluid is managed semi-implicitly [6], so that no spurious power is injected by the coupling.

Without any boundary stabilization, the solution blows up around $t = 0.34$, when the backflow starts at the first open boundary (see also Fig. 1). The stabilized results are presented in Figs. 10–11, showing the snapshots of the velocity vectors on the different Neumann boundaries Γ_1–Γ_4, at a selected instant during backflow. In each case, we report the results obtained with the Stokes-residual stabilization (with Poiseuille and dynamics resistance approximations) computing the stabilization parameter ℓ_k^e using Equation (24) and taking $\sigma_k = 0.002$ and $\sigma_k = 0.0005$ ($k = 1\ldots, 4$), for the coarse and fine meshes, respectively. The two approaches for computing the open boundary pressure gradient produce similar results.

For this example, the analytical solution is not available and the approaches can only be compared on a qualitative level. For comparisons, we also report in Figs. 10–11 (bottom) the results of a Stokes simulation, in order to show that the stabilized Navier–Stokes solution is qualitatively and quantitatively different from a Stokes flow, confirming that the proposed stabilization term acts only as a regularization. In particular, we observe that the boundary velocity profiles obtained with the stabilized formulation (8) are in general non-symmetric, which might be a result of the shape of the three-dimensional domain near the boundary.

We observe that also in this example, where the physical convection term does not vanish (unlike in the case of the Womersley flow) we were able to reduce the stabilization parameter when decreasing the characteristic mesh element size.

As a further comparison, Fig. 12 depicts the estimated pressure gradients at all four open boundaries, confirming that the two resistance approximations yields very similar profiles. Moreover, note that the frequency content of the pressure gradient is relatively high. Hence, the direct computation of a time-dependent stabilizing velocity profile, which is needed for some of the methods based on a corrected Neumann boundary condition, i.e. [10,22,24,25] (see also Section 1) could be a challenging issue.
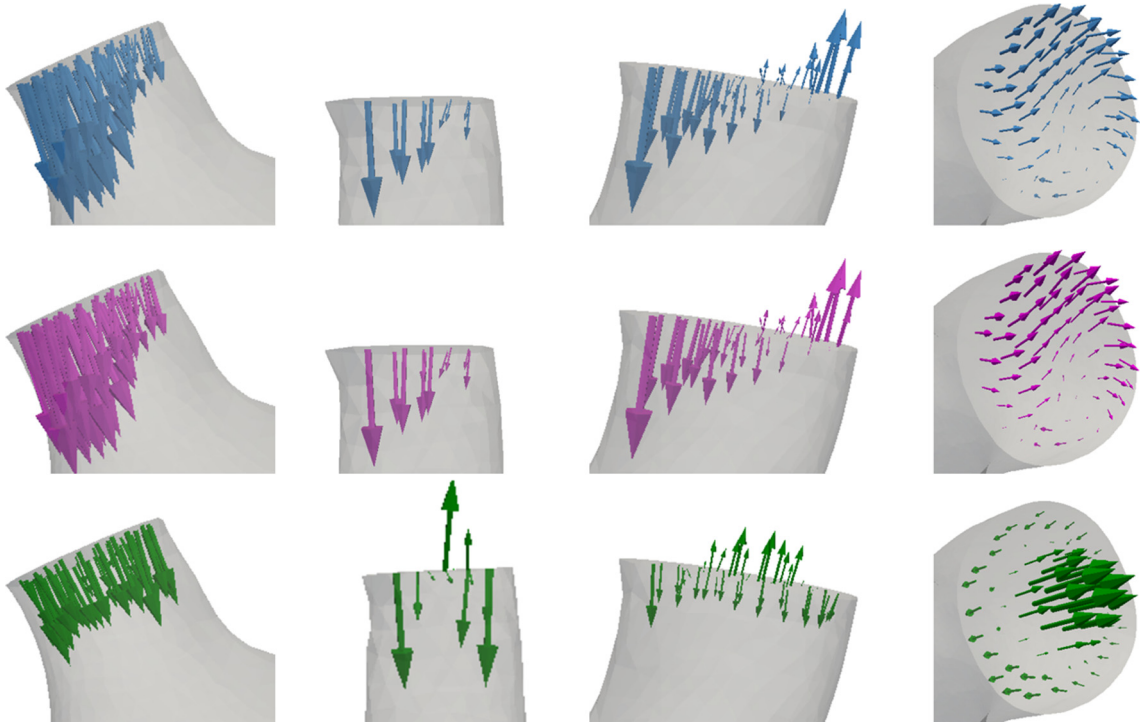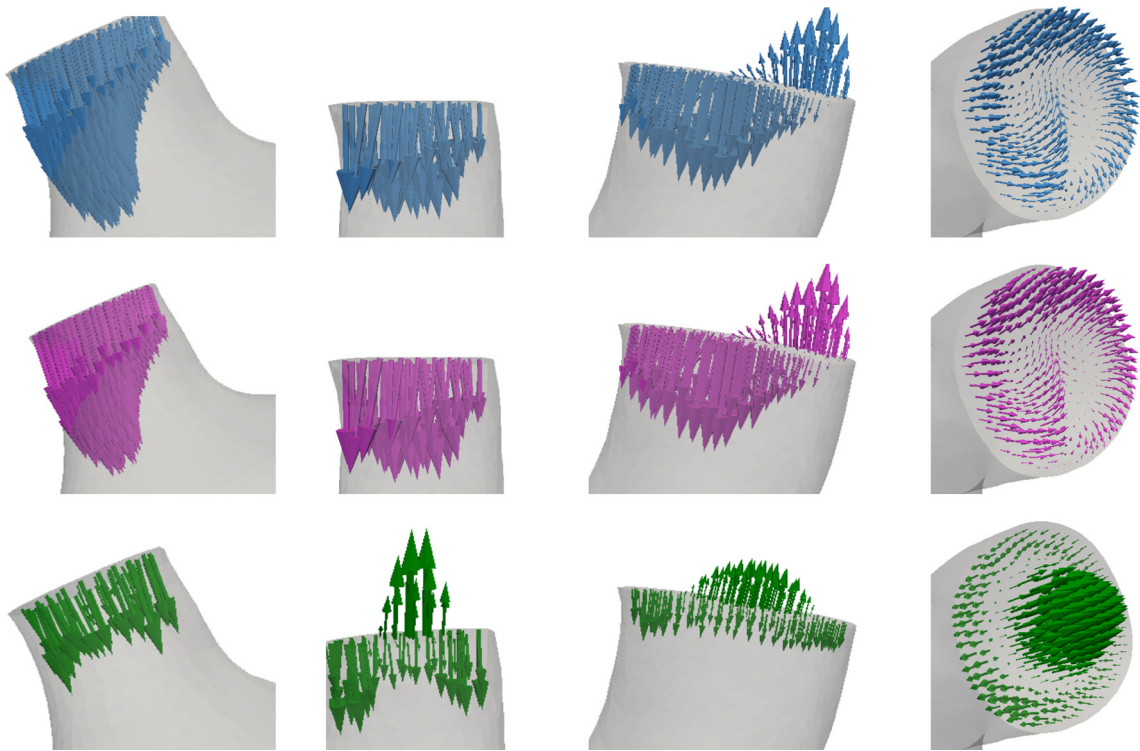
Fig. 10. Results of the stabilized formulation for the patient-specific aorta (coarse mesh). From left to right: Γ_1 ($t = 0.36$ s), Γ_2 ($t = 0.36$ s), Γ_3 ($t = 0.36$ s), Γ_4 ($t = 0.64$ s). Top: Stokes-residual stabilization ($\sigma = 0.002$) with Poiseuille resistance (cyan); middle: Stokes-residual stabilization ($\sigma = 0.002$) with dynamic resistance (magenta); bottom: results of a Stokes simulation (green). (For interpretation of the references to color in this figure legend, the reader is referred to the web version of this article.)

Fig. 11. Results of the stabilized formulation for the patient-specific aorta (fine mesh). From left to right: Γ_1 ($t = 0.36$ s), Γ_2 ($t = 0.36$ s), Γ_3 ($t = 0.36$ s), Γ_4 ($t = 0.64$ s). Top: Stokes-residual stabilization ($\sigma = 0.0005$) with Poiseuille resistance (cyan); middle: Stokes-residual stabilization ($\sigma = 0.0005$) with dynamic resistance (magenta); bottom: results of a Stokes simulation (green). (For interpretation of the references to color in this figure legend, the reader is referred to the web version of this article.)
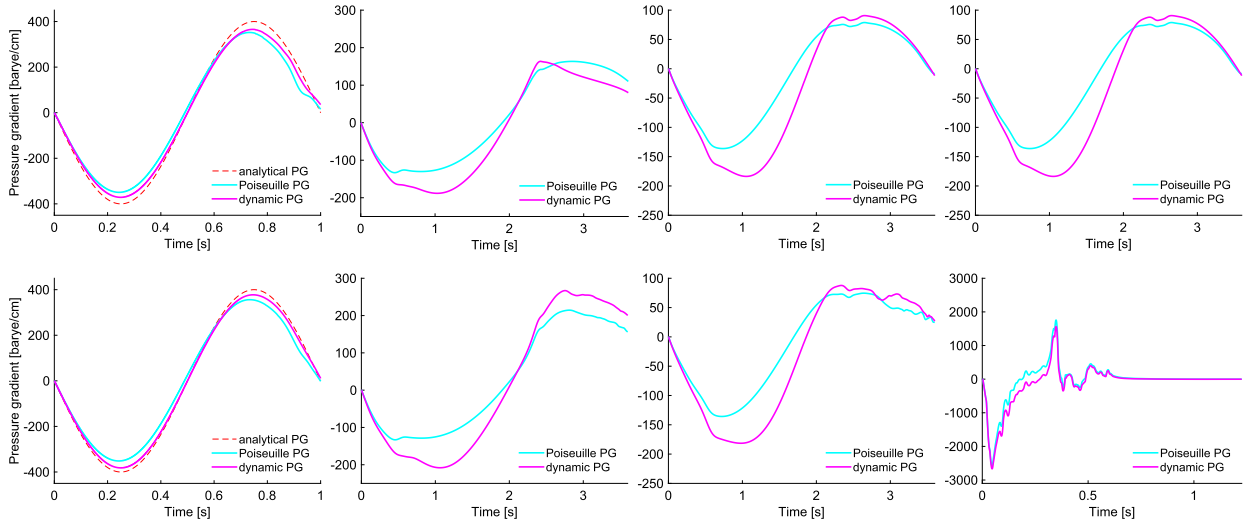
Fig. 12. Patient-specific aorta: approximated open boundary pressure gradients at the four open boundaries ($\Gamma_1, \ldots, \Gamma_4$, from left to right), comparing the Poiseuille resistance approximation (cyan) and dynamic resistance approximation (magenta). Top: coarse mesh. Bottom: fine mesh. (For interpretation of the references to color in this figure legend, the reader is referred to the web version of this article.)
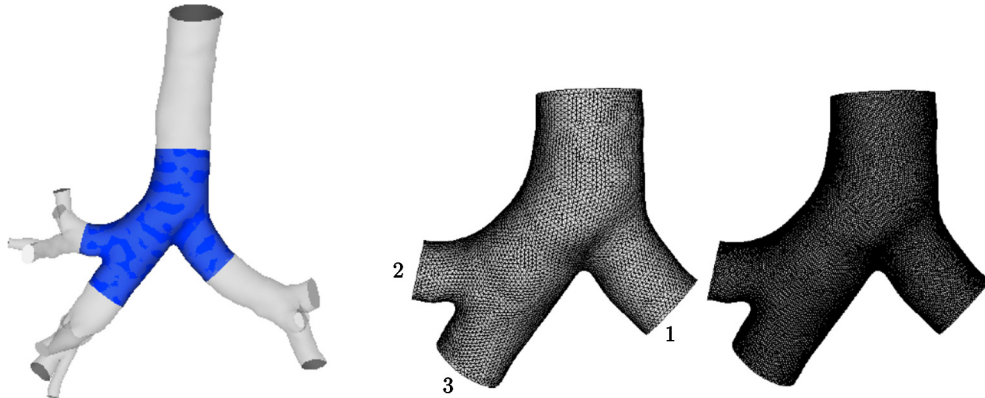

Fig. 13. Left: The original geometry of respiratory tract (grey) and the computational domain used for the simulation (blue). Right: The computational meshes: coarse (characteristic size $h = 0.11$) and fine (characteristic size $h = 0.055$). (For interpretation of the references to color in this figure legend, the reader is referred to the web version of this article.)

Finally, in Table 1 we report also the maximum values of the boundary resistance due to the stabilization term, for both the Poiseuille and dynamic approximations for the coarse mesh. In particular, for each outlet, these values ($\ell_k^e r_k^{pois}$ and $\ell_k^e r_k^{dyn}$, respectively) are below the corresponding proximal resistances R_k^p, hence fulfilling the stability condition (23) of Corollary 1. The inequality (23) is satisfied also for the fine mesh, as the stabilization parameter σ has been decreased of a factor of four, while the boundary resistances remain of the same order, as it can be seen from the approximated pressure gradients in Fig. 12.

4.2. Respiratory flow in a pulmonary tract geometry

Finally, we consider a respiratory flow in a realistic pulmonary tract with three open boundaries (Fig. 13), obtained as a section of a geometry recovered from medical imaging [18]. For the numerical simulations, we then considered two different level of refinement, denoted in what follows as the *coarse* (characteristic size $h = 0.11$) and the *fine* (characteristic size $h = 0.055$) mesh.

To set up the simulations, we first simulated a Stokes flow driven by a periodic imposed inlet pressure, with period $T = 4$ s. On the one hand, this step allowed to calibrate the parameters of the open boundary Windkessel models in order to obtain a physiological flow split between right and left lungs (about 40% and 60%, respectively). On the other hand, from the Stokes simulation we recovered a smooth inlet flow profile consistent with the geometry and the considered flow split, that was used as Dirichlet boundary condition on the velocity for the Navier–Stokes simulation. In this configuration, the peak backflow Reynolds number at the inlet reaches $Re = 1200$.
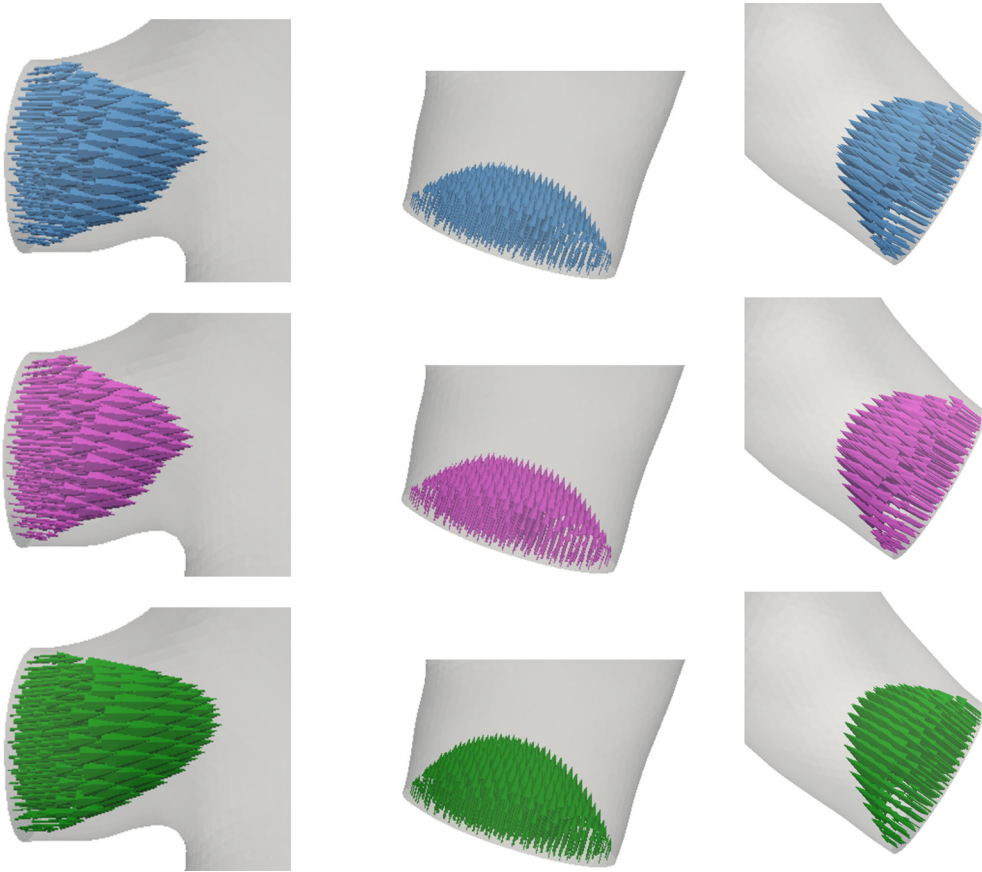
Fig. 14. Velocity profiles at the three open boundaries of the pulmonary tract at peak backflow ($t = 3.4$ s) for the coarse mesh ($h = 0.12$). Top: Stokes-residual stabilization ($\sigma = 0.002$) with Poiseuille resistance; middle: Stokes-residual stabilization ($\sigma = 0.002$) with dynamic resistance (magenta); bottom: solution of a Stokes problem (green). (For interpretation of the references to color in this figure legend, the reader is referred to the web version of this article.)

At the open boundaries, purely resistant lumped parameter models have been used, i.e. $P_k = R_k^p Q_k$ in (1), with $R_1^p = 10$ g/(s cm^4), $R_2^p = R_3^p = 15$ g/(s cm^4).

Without any stabilization the solution blows up during backflow. The following figures show the numerical results using the Stokes-residual stabilization, comparing the two levels of refinement and the two approaches for computing the boundary pressure gradient.

The stabilization parameter for the Stokes-residual method was also computed using equation (24) with $\sigma_k = 0.002$ and $\sigma_k = 0.0005$ ($k = 1, 2, 3$) for the coarse and fine meshes, respectively.

Figs. 14–15 show the open boundary velocity field at selected instants for the coarse and fine mesh, respectively, while Fig. 16 depicts the pressure gradients at the different open boundaries for the Stokes-residual stabilization, using the two approaches for the pressure gradient approximation.

Note that, also in this case, the simulations remain stable using the Stokes-residual stabilization, with the stabilization parameter σ derived from the Womersley flow simulation. We also observe that the solution is more similar to the Stokes flow, than in the previous example (blood flow in the ascending aorta). This difference might not be only due to the backflow stabilization but on the lower frequency content of the input data.

Finally, in Table 2 we report the maximum values of the boundary resistances due to the stabilization term (for the coarse mesh), compared with the corresponding proximal resistances of the physical LPM. Also in this case, both the terms $\ell_k^e r_k^{pois}$ and $\ell_k^e r_k^{dyn}$ are smaller than the physical resistances, hence fulfilling the stability condition (23). As in the case of the aortic geometry, the inequality holds also for the fine mesh, as the stabilization parameter σ has been decreased, while the boundary resistances are of the same order as in the case of the coarse mesh (see, e.g., the approximated boundary pressure gradients in Fig. 16).

5. Conclusions

We proposed a stabilization term for the incompressible Navier–Stokes equations proportional to the residual of a Stokes problem on the boundary, in order to handle backflow instabilities at open (Neumann) boundaries. The approach has the
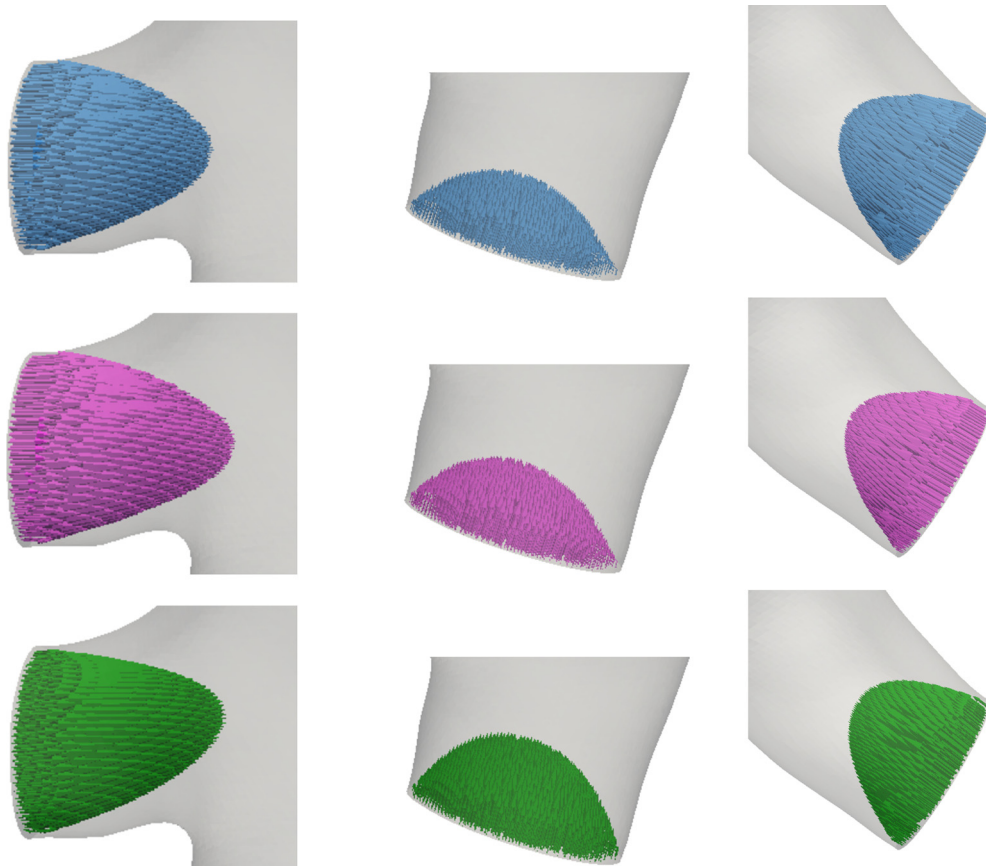
Fig. 15. Velocity profiles at the three open boundaries of the pulmonary tract at peak backflow ($t = 3.4$ s) for the fine mesh ($h = 0.06$). Top: Stokes-residual stabilization ($\gamma = 0.0005$) with Poiseuille resistance; middle: Stokes-residual stabilization ($\gamma = 0.0005$) with dynamics resistance (magenta); bottom: solution of a Stokes problem (green). (For interpretation of the references to color in this figure legend, the reader is referred to the web version of this article.)
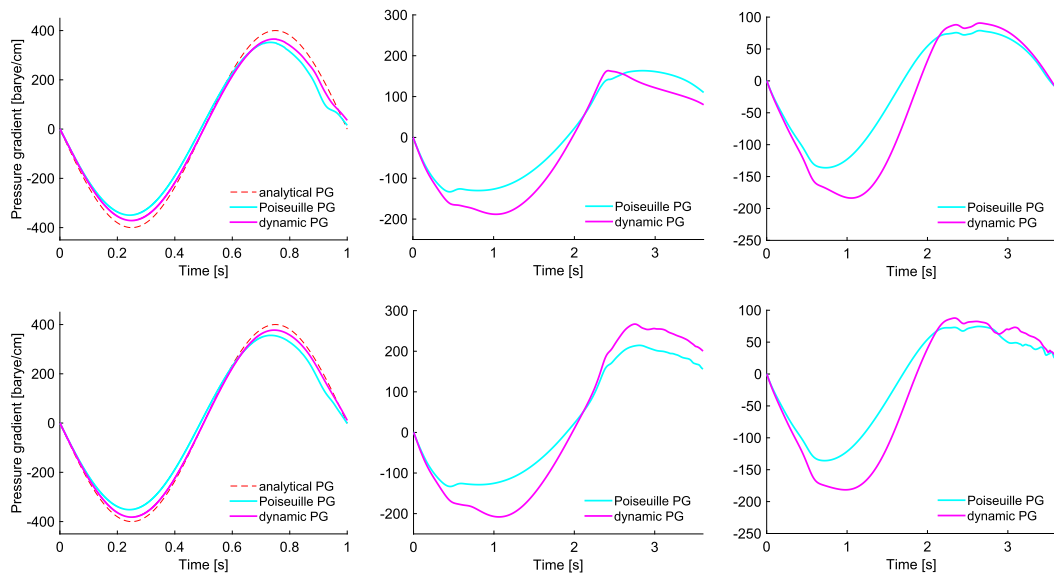
Fig. 16. Pulmonary tract: approximated open boundary pressure gradients at the four open boundaries ($\Gamma_1, \ldots, \Gamma_3$, from left to right), comparing the Poiseuille resistance approximation (cyan) and dynamic resistance approximation (magenta). Top: coarse mesh. Bottom: fine mesh. (For interpretation of the references to color in this figure legend, the reader is referred to the web version of this article.)

Table 2
The proximal resistances for the bronchial geometry (first row) and the maximum values over time of the resistances due to the stabilization term, using the Poiseuille and dynamics approximations (second and third row, respectively).

	Γ_1	Γ_2	Γ_3
R^p [g/(s cm^4)]	10	15	15
$\max_t\{\ell_k^e\, r_k^{\mathrm{pois}}\}$ [s^2 cm^4/g]	0.38	1.34	0.21
$\max_t\{\ell_k^e\, r_k^{\mathrm{dyn}}\}$ [s^2 cm^4/g]	0.35	1.01	0.23

advantages that it does not require modifications (e.g., extensions) of the computational domain nor a priori information about the shape of the solution. Moreover, it is based on the computation of few additional boundary integrals, hence adding only a negligible additional computational cost to a standard finite element method. The performance of the method has been assessed through several numerical tests. First, we considered a transient Womersley flow in blood and airflow regimes, in which the numerical results have been compared with a stable reference solution. For both regimes, the numerical results showed that the Stokes-residual stabilization outperforms previously reported methods in terms of accuracy. As next, we applied the stabilization to the simulation of physiologically realistic aortic and bronchial geometries obtained from medical imaging. In all cases, the results show that the size of the stabilization parameter may be decreased with the mesh size.

Acknowledgements

References

[1] D. Barber, E. Oubel, A. Frangi, D. Hose, Efficient computational fluid dynamics mesh generation by image registration, Med. Image Anal. 11 (2007) 648–662.
[2] Y. Bazilevs, J. Gohean, T. Hughes, R. Moser, Y. Zhang, Patient-specific isogeometric fluid-structure interaction analysis of thoracic aortic blood flow due to implantation of the Jarvik 2000 left ventricular assist device, Comput. Methods Appl. Mech. Eng. 198 (2009) 3534–3550.
[3] C. Bègue, C. Conca, F. Murat, O. Pironneau, A nouveau sur les équations de Stokes et de Navier–Stokes avec des conditions aux limites sur la pression, C. R. Acad. Sci., Ser. 1 Math. 304 (1987) 23–28.
[4] C. Bertoglio, Forward and inverse problems in fluid-structure interaction. Application to hemodynamics, Ph.D. thesis, Université Pierre et Marie Curie, Paris VI, 2012, http://tel.archives-ouvertes.fr/tel-00768188.
[5] C. Bertoglio, A. Caiazzo, A tangential regularization method for backflow stabilization in hemodynamics, J. Comput. Phys. 261 (2014) 162–171, http://dx.doi.org/10.1016/j.jcp.2013.12.057.
[6] C. Bertoglio, A. Caiazzo, M. Fernández, Fractional-step schemes for the coupling of distributed and lumped models in hemodynamics, SIAM J. Sci. Comput. 35 (2013) B551–B575, http://dx.doi.org/10.1137/120874412.
[7] P.J. Blanco, S. Deparis, A.C.I. Malossi, On the continuity of mean total normal stress in geometrical multiscale cardiovascular problems, J. Comput. Phys. 251 (2013) 136–155.
[8] M. Braack, P.B. Mucha, Directional do-nothing condition for the Navier–Stokes equations, J. Comput. Math. 32 (2014) 507–521.
[9] A. Brooks, T. Hughes, Streamline upwind/Petrov–Galerkin formulations for convection dominated flows with particular emphasis on the incompressible Navier–Stokes equations, Comput. Methods Appl. Mech. Eng. 32 (1982) 199–259.
[10] C.H. Bruneau, P. Fabrie, Effective downstream boundary conditions for incompressible Navier–Stokes equations, Int. J. Numer. Methods Fluids 19 (1994) 693–705.
[11] C.H. Bruneau, P. Fabrie, New effective boundary conditions for incompressible Navier–Stokes equations: a well-posedness result, Modél. Math. Anal. Numér. 30 (1996) 815–840.
[12] A. Caiazzo, G. Montecinos, L.O. Müller, E.M. Haacke, E.F. Toro, Computational haemodynamics in stenotic internal jugular veins, J. Math. Biol. 70 (2015) 745–772.
[13] A. Chorin, On the convergence of discrete approximations to the Navier–Stokes equations, Math. Comput. 23 (1969) 341–353.
[14] A. Comerford, C. Förster, W.A. Wall, Structured tree impedance outflow boundary conditions for 3d lung simulations, J. Biomech. Eng. 132 (2010) 081002.
[15] S. Dong, An outflow boundary condition and algorithm for incompressible two-phase flows with phase field approach, J. Comput. Phys. 266 (2014) 47–73.
[16] S. Dong, G. Karniadakis, C. Chrzssostomidis, A robust and accurate outflow boundary condition for incompressible flow simulations on severely-truncated unbounded domains, J. Comput. Phys. (2014) 83–105.
[17] M. Esmaily Moghadam, Y. Bazilevs, T.Y. Hsia, I. Vignon-Clementel, A. Marsden, Modeling of Congenital Hearts Alliance, A comparison of outlet boundary treatments for prevention of backflow divergence with relevance to blood flow simulations, Comput. Mech. 48 (2011) 277–291, http://dx.doi.org/10.1007/s00466-011-0599-0.
[18] C. Fetita, S. Mancini, D. Perchet, F.M.T. Prêteux, L. Vial, An image-based computational model of oscillatory flow in the proximal part of tracheobronchial trees, Comput. Methods Biomech. Biomed. Eng. 8 (2005) 279–293.
[19] L. Formaggia, J.F. Gerbeau, F. Nobile, A. Quarteroni, Numerical treatment of defective boundary conditions for the Navier–Stokes equations, SIAM J. Numer. Anal. 40 (2002) 376–401.

[20] L. Formaggia, A. Quarteroni, A. Veneziani (Eds.), Cardiovascular Mathematics. Modeling and Simulation of the Circulatory System, Model. Simul. Appl., vol. 1, Springer, 2009.
[21] L. Formaggia, A. Quarteroni, C. Vergara, On the physical consistency between three-dimensional and one-dimensional models in haemodynamics, J. Comput. Phys. 244 (2013) 97–112.
[22] V. Gravemeier, A. Comerford, L. Yoshihara, M. Ismail, W. Wall, A novel formulation for Neumann inflow boundary conditions in biomechanics, Int. J. Numer. Methods Biomed. Eng. 28 (2012) 560–573, http://dx.doi.org/10.1002/cnm.1490.
[23] J.L. Guermond, P. Minev, J. Shen, An overview of projection methods for incompressible flows, Comput. Methods Appl. Mech. Eng. 195 (2006) 6011–6045.
[24] M. Ismail, V. Gravemeier, A. Comerford, W. Wall, A stable approach for coupling multidimensional cardiovascular and pulmonary networks based on a novel pressure-flow rate or pressure-only Neumann boundary condition formulation, Int. J. Numer. Methods Biomed. Eng. 30 (2014) 447–469.
[25] H. Kim, C. Figueroa, T. Hughes, K. Jansen, C. Taylor, Augmented Lagrangian method for constraining the shape of velocity profiles at outlet boundaries for three-dimensional finite element simulations of blood flow, Comput. Methods Appl. Mech. Eng. 198 (2009) 3551–3566.
[26] M. Kim, R. Bordas, W. Vos, R.A. Hartley, C.E. Brightling, D. Kay, V. Grau, K.S. Burrowes, Dynamic flow characteristics in normal and asthmatic lungs, Int. J. Numer. Methods Biomed. Eng. 31 (12) (2015), http://dx.doi.org/10.1002/cnm.2730.
[27] J. Oakes, A.L. Marsden, C. Grandmont, C. Darquenne, I. Vignon-Clementel, Distribution of aerosolized particles in healthy and emphysematous rat lungs: comparison between experimental and numerical studies, J. Biomech. 48 (2015) 1147–1157, http://dx.doi.org/10.1016/j.jbiomech.2015.01.004.
[28] J. Oakes, A.L. Marsden, C. Grandmont, S.C. Shadden, C. Darquenne, I. Vignon-Clementel, Airflow and particle deposition simulations in health and emphysema: from in vivo to in silico animal experiments, Ann. Biomed. Eng. 42 (2014) 899–914, http://dx.doi.org/10.1007/s10439-013-0954-8, https://hal.archives-ouvertes.fr/hal-00916348.
[29] A. Porpora, P. Zunino, C. Vergara, M. Piccinelli, Numerical treatment of boundary conditions to replace lateral branches in hemodynamics, Int. J. Numer. Methods Biomed. Eng. 28 (2012) 1165–1183.
[30] A. Quarteroni, S. Ragni, A. Veneziani, Coupling between lumped and distributed models for blood flow problems, Comput. Vis. Sci. 4 (2001) 111–124.
[31] Y. Shi, P. Lawford, R. Hose, Review of zero-d and 1-d models of blood flow in the cardiovascular system, Biomed. Eng. Online 10 (2011) 33.
[32] H. Si, Adaptive tetrahedral mesh generation by constrained Delaunay refinement, Int. J. Numer. Methods Eng. 75 (2008) 856–880.
[33] R. Temam, Une méthode d'approximation de la solution des équations de Navier–Stokes, Bull. Soc. Math. Fr. 96 (1968) 115–152.
[34] I.E. Vignon-Clementel, C.A. Figueroa, K.E. Jansen, C.A. Taylor, Outflow boundary conditions for 3d simulations of non-periodic blood flow and pressure fields in deformable arteries, Comput. Methods Biomech. Biomed. Eng. 13 (2010) 625–640.
[35] D. Young, S.E. Lamb, S. Shah, I. MacKenzie, W. Tunnicliffe, R. Lall, K. Rowan, B.H. Cuthbertson, High-frequency oscillation for acute respiratory distress syndrome, N. Engl. J. Med. 368 (2013) 806–813.